Thermal and magnetic evolution of Mercury with a layered Fe-Si(-S) core

Christopher J. Davies [a],[*], Anne Pommier [b], Sam Greenwood [a], Alfred Wilson [a]

[a] *School of Earth and Environment, University of Leeds, Leeds LS2 9JT, UK*
[b] *Earth and Planets Laboratory, Carnegie Institution for Science, Washington, DC, USA*

ARTICLE INFO

ABSTRACT

Elucidating the structure and composition of Mercury is important for understanding its interior dynamics and evolution. The planet is characterised by unusual chemical characteristics and a weak magnetic field generated in a large metallic core, and its early evolution was also marked by the presence of a magnetic field, widespread volcanism and global contraction. Here we develop a parameterised model of coupled core-mantle thermal and magnetic evolution considering a layered Fe-Si(-S) core structure with chemical and physical properties of the mantle and the core based on previous laboratory studies. We seek successful solutions that are consistent with observations of Mercury's long-lived dynamo, total global contraction, present-day crustal thickness, and present-day interior structure. Successful solutions have a mantle reference viscosity $> 10^{21}$ Pa s (corresponding to a present-day bulk mantle viscosity $> 2 \times 10^{20}$ Pa s), a silicon concentration in the core > 13 wt%, a present inner core radius of $\sim 1000 - 1200$ km and a thermally stable layer $\sim 500 - 800$ km thick below the core-mantle boundary. Our results show that if present, a molten FeS layer atop the core has minimal effect on Mercury's long-term thermal and magnetic evolution. Predictions from our models can be tested with upcoming Bepi-Colombo observations.

1. Introduction

The MErcury Surface, Space ENvironment, GEochemistry, and Ranging (MESSENGER) mission has shown that Mercury currently generates a global magnetic field that is dominantly dipolar at the surface, approximately 100 times weaker than Earth's surface field (Anderson et al., 2011), and likely generated by a convection-driven dynamo in the core (Christensen, 2006; Manglik et al., 2010). Remanent crustal magnetization with an inferred age of $3.7 - 3.9$ billion years (Johnson et al., 2015) suggests that the dynamo operated in Mercury's early history. The similar bulk densities and different sizes of Earth and Mercury suggest that Mercury's dense core is large (e.g., Margot et al., 2018, and references therein), with a radius $r_c \sim 2000$ km (e.g., Hauck et al., 2013; Wardinski et al., 2019; Knibbe et al., 2021). Magnetic and geodetic measurements combined with the planet's bulk density reveal that the iron-rich core is at least partially liquid at present (e.g., Margot et al., 2007; Steinbrügge et al., 2021). The presence of a solid inner core has been inferred by several studies, with an estimated radius up to 1500 km (Knibbe and van Westrenen, 2018; Genova et al., 2019; Knibbe et al., 2021; Tao and Fei, 2021), depending on the assumed composition (Genova et al., 2019). These results are complemented by observations of widespread

shortening structures that represent up to 7 km of global contraction (Byrne et al., 2014; Watters, 2021) arising from planetary differentiation and secular cooling, and by a present crust thickness of 35 ± 18 km (Padovan et al., 2015) resulting from mantle melting and heat pipe volcanism (Peterson et al., 2021; Beuthe et al., 2020).

Most previous studies of Mercury's thermal evolution have assumed an Fe-S core (e.g. Hauck et al., 2004; Grott et al., 2011; Tosi et al., 2013). Sulphur is a common candidate in terrestrial cores because it is cosmochemically abundant and siderophile at certain redox conditions. However, low Fe and high S contents in Mercurian lavas suggest that the core formed under highly reducing conditions, 7 to 3 log units below the oxygen fugacity of the iron-wüstite equilibrium (McCubbin et al., 2012; Zolotov et al., 2013; Namur et al., 2016). At these conditions, only $\sim 1.5 - 2.0$ wt.% ($2.6 - 3.4$ at.%) sulphur is expected in the core (Boujibar et al., 2014; Namur et al., 2016). In contrast, a high Si content of ~4 wt.% (7.6 at.%) to ~20-25 wt.% (33-40 at.%) (Knibbe and van Westrenen, 2018; Goossens et al., 2022) and possibly a non-negligible amount of C is thought to have partitioned to the core (e.g., Vander Kaaden et al., 2020). At the pressure-temperature (PT) conditions of ~ 20 GPa and ~ 2000 K, i.e., deep in the core, Si partitions almost equally between solid and liquid metal (Tao and Fei, 2021), implying

that negligible gravitational energy is released in an Fe-Si core, and inner core growth helps to power the dynamo solely through latent heat release. In comparison, in an Fe-S core, S would partition strongly into the liquid (Kuwayama and Hirose, 2004) as the inner core grows, liberating gravitational energy that maintains dynamo action efficiently (Nimmo, 2015).

Knibbe and van Westrenen (2018) were the first to investigate the influence of an Fe-Si core on the thermal history of Mercury. In their solutions of parameterized coupled core-mantle evolution, the core-mantle boundary (CMB) heat flow rapidly falls below the heat conducted along the core adiabat, which leads to the growth of a thermally stratified layer downwards from the CMB and an attendant reduction in core cooling. Their results showed that long-lived dynamo action can be maintained in an Fe-Si core, powered by the early nucleation and slow growth of a solid inner core. Knibbe and van Westrenen (2018) found solutions that matched the present crustal thickness, but did not consider the global contraction. Several previous studies have obtained thermal histories consistent with a total contraction of $1 - 10$ km, but did not include the effect of a thermally stable layer and assumed an Fe-S core (Hauck et al., 2004; Grott et al., 2011; Tosi et al., 2013) or pure Fe core (Peterson et al., 2021). Given that inner core growth is the main contribution to global contraction (Grott et al., 2011) and that core chemistry and thermal stratification strongly affect its evolution (Knibbe and Van Hoolst, 2021), it is important to reconsider the Fe-Si core evolution.

In addition, the presence of a hypothetical FeS(-rich) layer has been suggested at the top of the core (Malavergne et al., 2010; Smith et al., 2012), and its estimated thickness ranges from < 15 km to $100 - 220$ km, depending on the S content of the accreting materials (Cartier et al., 2020; Malavergne et al., 2010; Pirotte et al., 2023). This layer is probably absent if it formed in equilibrium with the silicate part of a S-saturated Mercury (Cartier et al., 2020; Pirotte et al., 2023). However, the conditions of Mercury's differentiation and hence the origin and stability of the stoichiometric FeS layer are still poorly constrained. Phase equilibria experiments show that the upper portion of an Fe-Si-S core could be immiscible if the amount of Si is > 11 wt.% (> 20 at.%), producing an Fe-Si liquid coexisting with a less dense Fe-S liquid below the CMB (Fig. 1). Alternatively, the layer could have resulted from the differentiation of the silicate mantle, which is known to contain sulfides (e.g., Boukaré et al., 2019; Lark et al., 2022). If present, this FeS layer is probably liquid because the melting temperature of FeS at the CMB pressure of ~ 5 GPa is lower (< 1700 K; Urakawa et al., 2004) than the temperatures suggested by thermal evolution models (Knibbe and van Westrenen, 2018). Partitioning experiments have revealed that the layer could incorporate some heat-producing elements (HPEs), but this result would be inconsistent with Th/U ratios of Mercury's lavas (Pirotte et al., 2023). HPEs are expected to stay in the silicate portion of the planet (Boujibar et al., 2019; Pirotte et al., 2023). In any case, the influence of the FeS layer on the thermal evolution of Mercury's core remains to be investigated.

Using coupled core-mantle evolution models, our study aims to establish evolutionary scenarios under which the inferred global contraction, crustal thickness, and long-lived magnetic field can be matched simultaneously, thereby making predictions that can be tested using data from the BepiColombo mission.

2. Method

The model consists of 1D parameterisations of mantle-lithosphere and core evolution that are coupled at the CMB: mantle convection sets the heat extracted from the core, and the resultant change in CMB temperature influences the heat flux. An example of a 1D model is shown in Fig. 2. An adiabatic core temperature profile $T_{c,a}$ extends from the centre of the planet and intersects the core liquidus $T_{c,l}$ at the inner core boundary (ICB), radius r_i. $T_{c,a}$ is matched to a conductive profile $T_{c,s}$ at the base of the stably stratified layer, radius r_s. The conductive profile
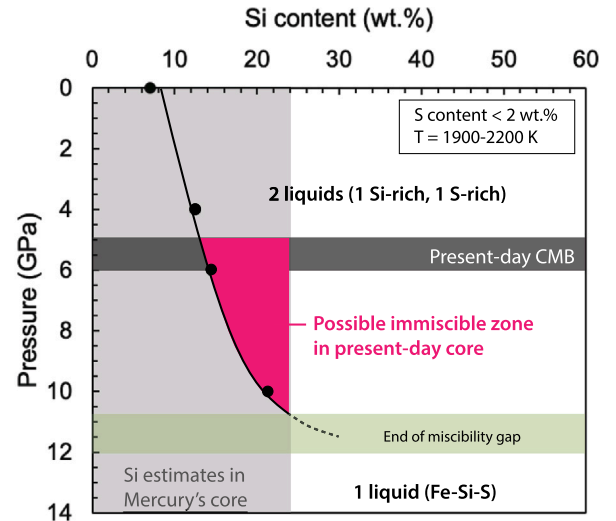

Fig. 1. Immiscibility in the Fe-Si-S core: Pressure vs. Si content showing the region of immiscibility at $1900 - 2200$ K, where Fe-S and Fe-Si liquids coexist. The bulk core composition considered has up to 25 wt.% Si and less than 2 wt.% S. Immiscibility ends between 10 and 12 GPa. Black circles are determined from the liquid miscibility gap in the laboratory-based ternary diagrams (Fe-FeS-FeSi) by Morard and Katsura (2010), considering less than 3 at.% S (~ 2 wt.%), in agreement with core composition estimates. The grey area shows the Si content in the core from Knibbe and van Westrenen (2018). The overlap between this grey area and the immiscibility limit suggests that for $T = 1900 - 2200$ K, Fe-S and Fe-Si liquids might coexist in the outer core up to about 11 GPa.

$T_{c,s}$ is matched to a new temperature profile at the base of the FeS layer, radius r_{FeS}, which continues to the CMB, radius r_c. The mantle temperature profile, denoted T_m, consists of a drop across the lower boundary layer directly above the CMB, a uniform temperature in the convective bulk, and further drops to the base of the lithosphere (radius r_l), crust (radius r_{cr}), and regolith (radius r_r). Mantle melting is determined by comparing T_m to the mantle liquidus $T_{m,l}$ and solidus $T_{m,s}$. The mantle-lithosphere parameterisation is identical to that used by Knibbe and van Westrenen (2018), who advanced the work of Grott et al. (2011). The core parameterisation follows the model of Greenwood et al. (2021a,b).

We adopt a simple representation of the FeS layer that can be readily included in the core evolution model. We consider an immiscible layer below the CMB (Fig. 1) that is entirely liquid since Knibbe and van Westrenen (2018) found that the CMB temperature exceeded 1700 K in almost all of their models, which is above the melting point of FeS at Mercury's core conditions (e.g., Morard and Katsura, 2010). This is confirmed by our results. We assume that vigorous core convection in Mercury's early history caused all of the S that initially entered the core to be rapidly processed through the immiscible region such that the initial configuration consists of an Fe-Si bulk below a pure FeS layer. We further assume that the FeS layer is lighter than the bulk Fe-Si core throughout Mercury's history and hence remains as a distinct layer below the CMB that is not disturbed by the underlying core convection. The important properties of the layer are its thickness D_{FeS} and thermal conductivity k_{FeS}. k_{FeS} is expected to be lower for FeS than Fe-Si alloys at Mercury's core conditions (Pommier et al., 2019). Low conductivity can stifle heat loss from the bulk core if the FeS layer is thermally stratified, but can also help maintain convection by reducing the adiabatic heat flow.

2.1. Mantle parameterisations

Mantle convection in Mercury is thought to operate in the stagnant lid regime (e.g., Tosi et al., 2013). The lithosphere includes a low
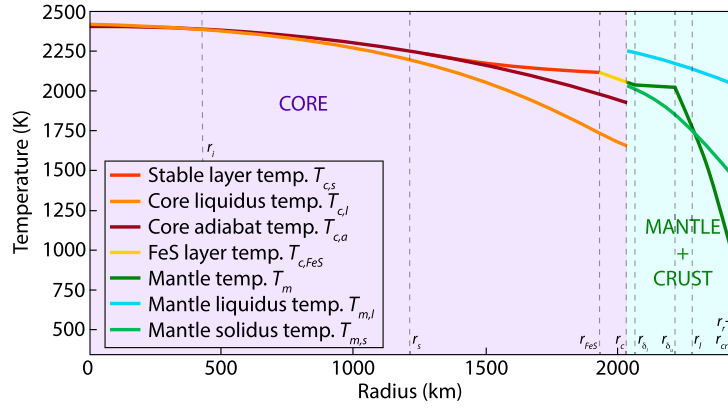
Fig. 2. Example of a 1D coupled core-mantle evolution model, showing the different radii and temperatures used in this study. Subscripts c and m denote the core and the mantle, respectively. In the core, the temperature profiles are the liquidus $T_{c,l}$, the adiabat $T_{c,a}$, the conductive profile in the thermally stable layer $T_{c,s}$, and the profile within the FeS layer $T_{c,FeS}$. The mantle temperature is simply denoted T_m, though it encompasses the convecting mantle, lithosphere, crust and regolith. The different radii correspond to the inner core boundary r_i, the base of the thermally stable layer r_s, the base of the FeS layer r_{FeS}, the core-mantle boundary r_c, the top (bottom) of the lower (upper) thermal boundary layer in the mantle r_{δ_l} (r_{δ_u}), the base of the lithosphere r_l, base of the crust r_{cr}, base of the regolith r_r, and planetary radius r_p. The solution shows an arbitrary time point using a reference mantle viscosity $\eta_0 = 10^{21.5}$ Pa s, an initial CMB temperature $T_{c,0} = 2000$ K and a Si concentration in the core of $c_{Si} = 0.15$ (i.e., 15 wt%).

density and low thermal conductivity crust, below a regolith with an ultra-low conductivity. The total energy equation determines the evolution of the mantle temperature T_m as

$$\rho_m C_m V_m (1 + St) \frac{dT_m}{dt} = -Q_{conv} - Q_{hp} + Q_r + Q_{cmb}. \tag{1}$$

Here Q_{conv} is the heat lost from the convecting mantle into the base of the stagnant lid, Q_{hp} is the heat lost due to heat pipe volcanism, Q_r is the heat released from the decay of radiogenic elements U, Th, and K (see Appendix B), and Q_{cmb} is the heat extracted from the core at the CMB. The left-hand side represents mantle secular cooling including the latent heat release/consumption due to freezing/melting; ρ_m, C_m, and V_m are respectively the density, specific heat capacity, and volume of the bulk mantle. The Stefan number $St = (L_m V_a / C_m V_m) dm_a / dT_m$, where m_a is the average fraction of melt in the volume V_a where melt is present (see Appendix A). Q_{conv} and Q_{cmb} are both estimated using standard boundary layer theory (Knibbe and van Westrenen, 2018). The upper and lower thermal boundary layer thicknesses, denoted δ_u and δ_l, respectively, depend sensitively on mantle viscosity η, which is assumed to take the form

$$\eta = \eta_0 \exp\left(\frac{A(T_{ref} - T_m)}{RT_{ref} T_m}\right), \tag{2}$$

where η_0 is the reference viscosity at temperature $T_{ref} = 1600$ K, $A = 3 \times 10^5$ J mol^{-1} is the activation energy, and R is the gas constant. We check whether mantle convection persists to the present day (as it should in order to be consistent with the modelling assumptions) by comparing the sum of the boundary layer thicknesses to the depth d of the convecting mantle. Assuming standard boundary layer theory, $d/(\delta_u + \delta_l) \approx d/(2\delta) = Nu$ and the Nusselt number Nu, the ratio of total to conducted heat flow, tends to 1 as $(\delta_u + \delta_l) \to d$.

The growth of the stagnant lid and the heat Q_{hp} both depend on the crustal growth rate, which is given by

$$\frac{dD_{cr}}{dt} = u m_a \frac{V_a}{4\pi r_p^2}, \tag{3}$$

(see Appendix A) where D_{cr} is the crustal thickness and $r_p = 2440$ km is the planetary radius. $u = u_0 (Ra/Ra_c)^{2/3}$ is a parameterized convective velocity (see Knibbe and van Westrenen, 2018) with $Ra_c = 450$ the critical value of the Rayleigh number Ra. The time $t_{m,e}$ when melting ends is determined by $dD_{cr}/dt = 0$.

2.2. Core parameterisations

The FeS layer is considered part of the core. In the absence of this layer, the core is composed of an Fe-Si alloy and is initially entirely liquid and convecting everywhere, i.e. at the CMB, Q_{cmb} exceeds the adiabatic heat flow $Q_a(r_c)$, where

$$Q_a(r) = -4\pi r^2 k_c(r) \frac{\partial T_{c,a}}{\partial r} = 4\pi r^2 k_c(r) \frac{\alpha_c(r) g(r) T_{c,a}(r)}{C_c}. \tag{4}$$

In Eq. (4), α_c and C_c are the thermal expansivity and specific heat capacity of the core, g is gravitational acceleration, and $k_c(r)$ is the core thermal conductivity. Once the CMB heat flow becomes sub-adiabatic ($Q_{cmb} < Q_a$), a thermally stratified layer grows downwards into the liquid core. We check that this condition always arises first at the CMB. The inner core begins to grow once the core temperature cools to the melting point of the iron alloy at the centre of the planet. Our numerical implementation can account for top-down freezing in the "iron snow" regime (Dumberry and Rivoldini, 2015; Davies and Pommier, 2018), but this regime does not occur with the melting curves and adiabats considered.

The inner core and convection zone are assumed to be hydrostatic, adiabatic, and chemically well-mixed, as expected for vigorous convection (e.g., Nimmo, 2015). The thermal regime of Mercury's inner core (convecting vs. conducting) is unknown, but calculations indicate that the difference between the two regimes does not significantly affect the results (Rivoldini et al., 2009). The stable layer temperature profile $T_{c,s}$ is obtained by solving the 1D conduction equation allowing for radially varying thermal diffusivity (Greenwood et al., 2021a) and matches smoothly to the bulk adiabatic profile. With these assumptions and neglecting small terms, the core heat balance is given by (Nimmo, 2015; Greenwood et al., 2021a)

$$Q_{cmb} = \underbrace{-\int \rho_c C_c \frac{dT}{dt} dV}_{Q_s} + \underbrace{4\pi r_i^2 \rho_c L_c \frac{dr_i}{dt}}_{Q_L}, \tag{5}$$

where Q_s is the secular cooling, and Q_L is the latent heat released on freezing of the inner core. Here ρ_c and L_c are respectively the density and latent heat coefficient of the Fe-Si region (assumed constant). There is no gravitational energy released by inner core freezing as Si partitions evenly between solid and liquid phases. As a result, and assuming no mass flux at the CMB, the Si concentration of the core does not vary with time. Radiogenic heating is neglected since HPEs partition strongly into

the mantle (Malavergne et al., 2010; Pirotte et al., 2023) and have little effect on core evolution (Tosi et al., 2013).

Using the same assumptions as for equation (5), the entropy balance can be written

$$E_J + E_k = E_s + E_L, \tag{6}$$

where

$$E_J = \int \frac{\Phi}{T} dV, \quad E_k = \int k_c \left(\frac{\nabla T}{T}\right)^2 dV,$$

$$E_s = -\int \left(\frac{1}{T(r_c)} - \frac{1}{T}\right) \rho_c C_c \frac{dT}{dt} dV, \quad E_L = \left(\frac{1}{T(r_c)} - \frac{1}{T(r_i)}\right) Q_L.$$

Here E_s and E_L are the entropy contributions due to secular cooling and latent heat, respectively, E_k is the entropy produced by thermal conduction, and E_J is the entropy production due to dynamo action where Φ is the ohmic heating. Note that in equations (5) and (6) the temperature T is given by the adiabatic value $T_{c,a}$ in the inner core and convecting region, by $T_{c,s}$ in the stable layer, and by $T_{c,FeS}$ in the FeS layer.

Depending on the model parameters, the FeS layer can either be unstable ($Q_{cmb} > Q_a(r_c)$) or stable ($Q_{cmb} < Q_a(r_c)$) to thermal convection. The two scenarios, named "convecting FeS" and "conducting FeS", respectively, are treated separately by checking *a posteriori* that the FeS layer remains either stable or unstable for the whole of time. The stability of the layer can change over time. However, numerical difficulties arise when the temperature profiles switch between adiabatic and conductive, and therefore we have not pursued this further. The region below the FeS layer can switch from convective to conductive as determined by evaluating the total and adiabatic heat flow at r_{FeS}.

Convecting FeS: Initially the bulk and FeS regions are unstable and thus, taken to be well mixed and isentropic. Ignoring thin thermal boundary layers at r_{FeS}, the temperature and cooling rate are continuous across the core. Evaluation of equation (5) can then be split into two equations. The heat leaving the Fe-Si region, Q_{FeS}, is

$$Q_{FeS} = -\int \rho_c C_c \frac{dT}{dt} dV_{bulk} + 4\pi r_i^2 \rho_c L_c \frac{dr_i}{dt}, \tag{7}$$

where V_{bulk} is the volume of the Fe-Si region. The secular cooling of the FeS layer is obtained from

$$Q_s^{FeS} = -\int \rho_{FeS} C_{FeS} \frac{dT}{dt} dV_{FeS} = Q_{cmb} - Q_{FeS}, \tag{8}$$

where ρ_{FeS}, C_{FeS} and V_{FeS} are the density, specific heat capacity and volume of the FeS layer. When Q_{FeS} falls below the adiabatic heat flow at r_{FeS}, the bulk region begins to stratify. The heat flow from the bulk region into the convecting FeS layer is then calculated from

$$Q_{FeS} = -k_c^- 4\pi r_{FeS}^2 \nabla T_{c,FeS}^-, \tag{9}$$

where the superscript '-' indicates the value is taken on the lower side of r_{FeS}. Q_s^{FeS} is then calculated from equation (8) using equation (9), from which the new FeS layer temperature is obtained. For the conduction solution in the stratified layer below the convecting FeS layer, the temperature is fixed to the value at r_{FeS} obtained from cooling of the FeS layer. The thermal conductivity in the FeS layer is set to the constant value k_{FeS}.

Conducting FeS: Numerical calculation of the conduction solution requires that material properties vary smoothly with radius, and hence we do not attempt to model the discontinuity in thermal diffusivity that would exist at the base of the FeS layer. Instead we represent the FeS layer as a thermal conductivity anomaly. The radial profile of thermal conductivity is written as

$$k_c(r) = k(r)(1 - a(r)) + a(r) k_{FeS} \tag{10}$$

where $k(r)$ is calculated from equation (14) below, k_{FeS} is the fixed conductivity of the FeS layer and

$$a(r) = \left[1 + \exp\left(\frac{-5(r - r_{FeS})}{\delta}\right)\right]^{-1}. \tag{11}$$

The function $a(r)$ defines a smooth transition in k_c with radius between the bulk core and the FeS layer. In the absence of an FeS layer, $a = 0$ and $k_c(r) = k(r)$. In the presence of an FeS layer, the a function ensures that k_c transitions from the value k_{FeS} in the FeS layer to the profile $k(r)$ in the bulk core across a transition width δ. Tests showed that $\delta \leq 20$ km produces oscillations in the radial heat flux that are localised around r_{FeS}. The oscillations can be damped by increasing grid resolution and have no discernible effect on the time evolution of the solution. However, to ensure that these oscillations are absent, we use a value of $\delta = 50$ km throughout.

The model solves equation (1) for the mantle temperature T_m and equation (5), which determines the core temperature T_c. The temperature at the base of the lithosphere, T_l, is scaled from T_m as $T_l = T_m - c(RT_m^2)/A$ where $c = 2.21$ is an empirical constant (Knibbe and van Westrenen, 2018). Thermal profiles in the crust and regolith are determined by solving 1D conduction equations. Calculations start at 4.5 billion years ago and proceed to the present day unless r_i and r_s come within 1 km of each other, which indicates the disappearance of the core convection zone – the calculation is then terminated early and omitted from subsequent analysis. For runs without an FeS layer, resolution testing with timesteps of 0.01, 0.1 and 1 Myrs and a radial grid of 60, 40 and 20 points in the stable layer has verified that the latter is sufficient to obtain converged solutions. The addition of the FeS layer requires greater numerical resolution to resolve thermal gradients at r_{FeS}; for these calculations we use a timestep of 0.1 Myrs and 120 points in the stable layer region below the FeS layer.

3. Model constraints and parameters selection

We compare model outputs to 4 observationally-derived characteristics: 1) the existence of a dynamo at the present day; 2) the existence of a dynamo at 3.8 Ga; 3) a present crustal thickness of $18 - 53$ km, and 4) a total global contraction of $1 - 10$ km. Model runs that match them are referred to as "successful" for convenience. Models should also be consistent with the inferred present-day mass, moment of inertia and longitudinal libration amplitude and this is done by prescribing the CMB radius and crust, mantle, and core densities (see below). In the following we describe the selection and implementation of the 4 observational constraints before discussing the input parameters that determine the model behaviour.

Constraints 1 and 2 are assessed through the dynamo entropy E_J, which must be positive at 3.8 Ga and the present for dynamo action. The minimum value of E_J required to maintain dynamo action is unknown because E_J depends on the magnetic field distribution throughout the core. A simple lower bound can be obtained using the formula of Gubbins (1975), which gives the Ohmic dissipation due to the observable part of the field. Confining attention to the axial dipole g_1^0 and quadrupole g_2^0 and assuming the values from Wardinski et al. (2019), an electrical conductivity of 5×10^5 S m^{-1} and a mean core temperature of 2000 K gives $E_J = 0.06$ MW K^{-1} for the axial dipole component, and $E_J \approx 1$ MW K^{-1} for the axial quadrupole component. Therefore the minimum value of E_J required to sustain the observable part of Mercury's field is around 1 MW K^{-1}. We use this value below, assuming it applies over all time. We calculate the evolution of magnetic field strength over time using the theory of Davidson (2013) (implemented following Davies et al. (2022) with a prefactor equal to 1), but do not use it as a condition for a successful model because current scaling laws (which estimate the field strength based on the assumed balance of forces in the dynamo) do not predict Mercury's anomalously weak field (Christensen, 2010; Davidson, 2013). The model also does not predict detailed characteristics of the field morphology that can only be investigated in fully dynamical simulations (e.g., Takahashi et al., 2019), though these currently do not operate at the physical conditions of planetary cores.

Table 1

Parameters to be varied in this study. Numbers in bold are reference values. The bottom section includes parameters that vary with the core Si concentration.

Quantity	Symbol	Units	Value	Reference
		Mantle		
Regolith thickness	D_{reg}	km	$1-\mathbf{5}$	Grott et al. (2011)
HPE mantle/crust	f_{HPE}	-	**0.33**, 0.1, 0.9	Padovan et al. (2015)
Mantle conductivity	k_m	W m^{-1} K^{-1}	$\mathbf{3}, 4, 5$	Hofmeister et al. (2009); Freitas et al. (2021); Zhang et al. (2019)
Reference viscosity	η_0	Pa s	10^{19-22}	Knibbe and van Westrenen (2018)
Initial temperature	$T_{m,0}$	K	$\mathbf{1700}-1900$	Knibbe and van Westrenen (2018)
		Core		
Initial CMB Temperature	$T_{c,0}$	K	$1800-2200$	Knibbe and van Westrenen (2018)
Si concentration	c_{Si}	-	$0.07-0.15$	Chabot et al. (2014)
FeS layer thickness	D_{FeS}	km	$5-100$	Malavergne et al. (2010)
FeS conductivity at CMB	k_{FeS}	W m^{-1} K^{-1}	$5-25$	Manthilake et al. (2019); Saxena et al. (2021); Hsieh et al. (2024)
FeS layer density	ρ_{FeS}	kg m^{-3}	4800	Nishida et al. (2011)
Core Density	ρ_c	kg m^{-3}	$7930-6600c_{Si}$	Knibbe and van Westrenen (2018)
CMB Radius	r_c	km	$1945+610c_{Si}$	Knibbe and van Westrenen (2018)
Mantle Density	ρ_m	kg m^{-3}	$2750+3800c_{Si}$	Knibbe and van Westrenen (2018)

Padovan et al. (2015) estimated crustal thickness D_{cr} using geoid-to-topography analysis under the assumption of Airy isostasy, a crustal density of $2700-3100$ kg m^{-3}, and northern hemisphere data. Their least and most conservative ranges are 35 ± 18 km and $30-35$ km respectively, while Sori (2018) found 26 ± 11 km. By correlating crustal thickness and mantle melt production, Beuthe et al. (2020) obtained $D_{cr} = 19\pm3$ km in the northern volcanic plains (low melt production) to $D_{cr} = 50 \pm 12$ km in the ancient Mg-rich region (high melt production). We take $D_{cr} = 35 \pm 18$ km to determine a successful model run, but also consider whether such models can match narrower ranges. Byrne et al. (2016) determined that nine major surface volcanic units were emplaced by ~3.5 Ga, suggesting an early termination of widespread mantle melting and therefore a waning of crustal production, though younger ages have also been suggested (Fassett, 2016). We check our calculations for a relatively early termination of melting, $t_{m,e}$. However, given the uncertainty on the absolute $t_{m,e}$ and the sensitivity of this value to model parameters, we do not require our models to match a termination time of 3.5 Ga exactly. Melting is not expected to proceed to the present day, consistent with surface observations that indicate absence of present-day volcanism.

Following Grott et al. (2011) we assume planetary contraction Δr arises from thermal expansion/contraction Δr_{th}, mantle melting Δr_m, and inner core growth Δr_{ic}: $\Delta r = \Delta r_{th} + \Delta r_m + \Delta r_{ic}$, where

$$\Delta r_{th} = \frac{1}{r_p^2}\int_0^{r_c} \alpha_c \left[T_c(r) - T_{c,0}(r)\right] r^2 dr + \frac{1}{r_p^2}\int_{r_c}^{r_p} \alpha_m \left[T_m(r) - T_{m,0}(r)\right] r^2 dr, \tag{12}$$

$$\Delta r_m = \frac{1}{f}\frac{\delta V}{V}\left[D_{cr} - D_{cr,0}\right], \quad \Delta r_i = \frac{\rho_L - \rho_S}{\rho_L}\frac{r_i^3}{3r_p^2}. \tag{13}$$

Here α_c and α_m are thermal expansivities for the core and mantle, subscript 0 denotes the initial time, f is the volume fraction of extractable crustal components, $\delta V/V$ is the volume change on melting, and ρ_L and ρ_S are the densities of liquid and solid iron evaluated at the radius of the ICB as it advances over time (Supplementary Information). In equation (12) we do not use the simplified expression for the core in Grott et al. (2011, their equation 6) as this assumes the temperature is adiabatic at all radii, which is not the case in our model. We also implemented the extensions to equations (12) and (13) derived in Peterson et al. (2021), but found the present-day results to differ by only a few percent.

Model parameters that are varied are listed in Table 1 and fixed parameters are listed in Table 2. Because our focus is on the core, we mainly vary parameters that determine core evolution and keep man-

Table 2

Key parameters fixed in this study. All values are taken from Knibbe and van Westrenen (2018) except those for $\delta V/V$ and f, which come from Grott et al. (2011). Other parameters not listed are taken from Knibbe and van Westrenen (2018). Subscript 0 denotes initial time.

Quantity	Symbol	Units	Value
		Mantle/Crust	
Planetary radius	r_p	km	2440
Crust Density	ρ_{cr}	kg m^{-3}	2800
Initial crust thickness	$D_{cr,0}$	km	5
Initial lid thickness	$D_{l,0}$	km	50
Crust conductivity	k_{cr}	W m^{-1} K^{-1}	3.75
Regolith conductivity	k_r	W m^{-1} K^{-1}	0.2
Mantle Expansivity	α_m	K^{-1}	2×10^{-5}
Mantle latent heat	L_m	J kg^{-1}	6×10^5
Mantle heat capacity	C_m	J kg^{-1} K^{-1}	1212
Crust heat capacity	C_{cr}	J kg^{-1} K^{-1}	1000
Convective velocity	u_0	m s^{-1}	2×10^{-12}
Volume change on melting	$\delta V/V$		0.05
Volume fraction of extractable crust	f		0.4
		Core	
CMB pressure	P_c	GPa	5
Expansivity	α_c	K^{-1}	9e-5, 85e9, 4.5
Heat capacity	C_c	J kg^{-1}K^{-1}	835
Liquidus	$T_{c,l}$	K	See text
Latent heat	L_c	J kg^{-1}	5×10^5

tle parameters fixed. When possible, fixed parameter values have been chosen to be consistent with inferences from interior structure models that assume an Fe-Si(-S) core (e.g., Hauck et al., 2013; Knibbe et al., 2021; Steinbrügge et al., 2021). However, this is not always possible because models make different assumptions regarding key properties of the planet, such as core composition and thermal structure.

The CMB radius and densities of the core, mantle and crust, are parameterised following Knibbe and van Westrenen (2018) to be consistent with estimates of Mercury's polar moment of inertia C and that of the silicate shell (mantle plus crust) C_m. We use the parameterisations of Knibbe and van Westrenen (2018) to maintain consistency with their mantle model such that the differences arising in the respective core models can be more readily understood. Knibbe and van Westrenen (2018) use $r_c = 1945 + 610c_{Si}$ (km), $\rho_c = 7930 - 6600c_{Si}$ (kg m^{-3}), $\rho_m = 2750 + 3800c_{Si}$ (kg m^{-3}) and ρ_{cr} constant. These parameterisations yield values of $C/Mr_p^2 = 0.344 - 0.352$ (where $M = 3.27 - 3.30\times 10^{23}$ kg is Mercury's mass) and $C_m/C = 0.401 - 0.412$ for the range of core Si concentrations considered, which are within the uncertainties of values calculated from Mercury's obliquity and longitudinal libration amplitude by Margot et al. (2012) and Bertone et al. (2021), but not the
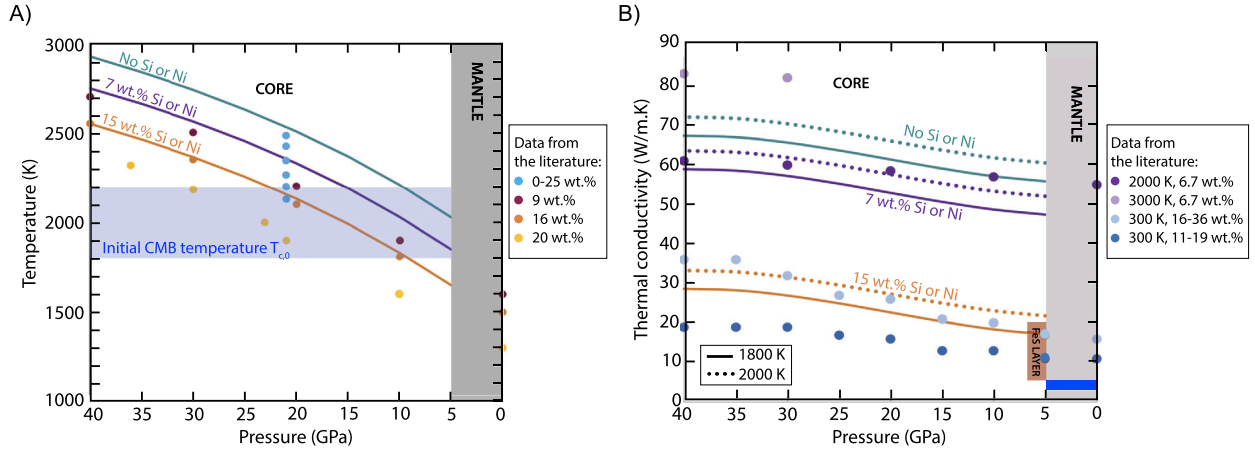
Fig. 3. Bulk core melting temperature $T_{c,l}$ (A) and thermal conductivity k (B) as a function of pressure for different compositions using the parameterisations given in equations (15) and (14), respectively. The circles correspond to the data from the literature used to develop these equations. The initial CMB temperature and the thermal conductivity of the mantle are indicated in blue. See the Supplementary Information for details.

values from Genova et al. (2019) (see Steinbrügge et al., 2021; Knibbe et al., 2021, for detailed discussions). We do not attempt to construct detailed interior structure models (e.g., Dumberry and Rivoldini, 2015; Steinbrügge et al., 2021) and take this general agreement as sufficient for our purpose of studying Mercury's thermal and magnetic evolution.

Mantle properties are mainly taken from Knibbe and van Westrenen (2018), who drew heavily from Grott et al. (2011). $\delta V/V$ is unknown and we use $\delta V/V = 0.05$, on the higher end of values from Grott et al. (2011), noting that larger values reduce contraction because mantle differentiation (which increases with $\delta V/V$) leads to planetary expansion. The varied mantle quantities in Table 1 are mostly unknown. The regolith thickness D_{reg} is varied in the range $1-5$ km, which are the upper and lower values in Grott et al. (2011). The crustal enrichment of HPEs, f_{HPE}, is varied in the range $0.1-0.9$, which is consistent with values from Padovan et al. (2015) ($0.1-0.33$) and Knibbe and van Westrenen (2018) ($0.1-0.9$). The mantle thermal conductivity k_m is varied in the range $3-5$ W m^{-1} K^{-1} with a default value of 3 W m^{-1} K^{-1}, which is consistent with values from thermal measurements on peridotite (Freitas et al., 2021) and silicates at relevant conditions, e.g., $2-5$ W m^{-1} K^{-1} for olivine (Fo90) from $400-1400$ K at $0-10$ GPa (Xu et al., 2004); $1.6-2.5$ W m^{-1} K^{-1} over $400-1800$ K for pyroxenes (Hofmeister et al., 2009). We consider a wide range of reference mantle viscosities $\eta_0 = 10^{19} - 10^{22}$ Pa s, which spans values estimated for wet and dry olivine (Grott et al., 2011). The initial mantle temperature $T_{m,0}$ is varied within the range of $\sim 1700-2100$ K considered by Knibbe and van Westrenen (2018). At first approximation, we consider that the likely presence of small amounts of carbon (Xu et al., 2024) do not affect mantle properties significantly.

Bulk core properties are generally taken from Knibbe and van Westrenen (2018). We vary the Si concentration c_{Si} and initial CMB temperature $T_{c,0}$. c_{Si} determines the CMB radius and bulk core density as described above and also influences the thermal conductivity k_c and melting point $T_{c,l}$. Previous studies have found $c_{Si} = 0-25$ wt.% (e.g., Hauck et al., 2013; Chabot et al., 2014; Margot et al., 2018; Vander Kaaden et al., 2020; Tao and Fei, 2021; Goossens et al., 2022). We consider $c_{Si} = 7-15$ wt.% Si, consistent with these recent works (Goossens et al., 2022). The upper end of this range is close to the eutectic composition (e.g., Fischer et al., 2013) and so the solids that form are denser than the residual liquid. The thermal conductivity of Fe-Si comes from De Koker et al. (2012) and Hsieh et al. (2020) for Fe-Si alloys containing $2-8$ wt.%Si, from $0-40$ GPa and $300-3000$ K. Using a least square regression, the data are adequately fit by a polynomial of the form

$$k = -0.1716c_{Si}^2 - 0.0059c_{Si} - 0.0004P^3 + 0.0266P^2 - 0.0654P$$
$$+ 0.0233T + 13.517 \tag{14}$$

with k in W m^{-1} K^{-1}, P in GPa, T in K, and the Si content in wt.%. The bulk core melting curve $T_{c,l}$ is constrained using experimental data on Fe-Si (Kuwayama and Hirose, 2004; Fischer et al., 2013) and Fe-Si-Ni (Dobrosavljevic et al., 2022) alloys. The data by Dobrosavljevic et al. (2022) for Fe-10Si-10Ni were extrapolated to pressures below 20 GPa using the pressure dependence of the melting temperature observed by Fischer et al. (2013) for Fe-9Si. The dataset considers $P = 0-60$ GPa and $T = 1300-3100$ K. For simplicity, we consider that the melting point depression due to Ni is comparable to that of Si. The best fit to the dataset is given by the polynomial

$$T_{c,l} = 0.0394c_{Si}^2 - 25.615c_{Si} + 0.0032P^3 - 0.5218P^2 + 43.325P + 1822.2$$

$$\tag{15}$$

with $T_{c,l}$ in K, c_{Si} in wt.%, and P in GPa. Profiles of $k(r)$ and $T_{c,l}(r)$ for different core compositions are shown in Fig. 3. The quality of the data fits are illustrated in the Supplementary Information.

For the FeS layer we fix its density $\rho_{FeS} = 4800$ kg m^{-3} (Nishida et al., 2011) and specific heat capacity $C_{FeS} = 800$ J Kg^{-1} K^{-1} and vary the layer thickness $D_{FeS} = r_c - r_{FeS}$ and thermal conductivity k_{FeS}. We assume that D_{FeS} is constant in time. This is expected firstly because the layer is unlikely to be remixed by core convection owing to its substantial density deficit compared to the bulk core. Moreover, given that pressure and composition in a given model are constant in time and the initial and final temperatures are comparable (see below and Knibbe and van Westrenen, 2018), we expect that any variations in layer size in our model due to changing thermodynamic conditions would be small. We vary D_{FeS} within the range $1-100$ km, which is equivalent to exploring 1-7 at.% S in the core.

Values for k_{FeS} are based on laboratory studies. Using direct thermal conductivity measurements in the solid state up to 42 GPa and 1023 K, Hsieh et al. (2024) showed that k_{FeS} ranges from $\sim 6-25$ W m^{-1} K^{-1}, increasing with both pressure and temperature. At 5 GPa and room temperature, k_{FeS} is about 7 W m^{-1} K^{-1}, and is expected to increase with temperature. Manthilake et al. (2019) and Saxena et al. (2021) measured the electrical resistivity of FeS at 8 and 2 GPa, respectively, in the solid and molten states. Using the Wiedemann-Franz law, Manthilake et al. (2019) predicted a value of $k_{FeS} = 4$ W m^{-1} K^{-1} for liquid FeS. In comparison, using an electrical resistivity value of 7×10^{-6} ohm m (Saxena et al., 2021) and a Sommerfeld value of 2.445×10^{-8} W Ω K^{-2}, the Wiedemann-Franz law provides a lower bound for molten FeS in the range $6.2-7.0$ W m^{-1} K^{-1} at $1800-2000$ K. These thermal conductivity values estimated from electrical measurements are slightly lower than that suggested by Hsieh et al. (2024) (> 7 W m^{-1} K^{-1}). This result implies that the lattice thermal conductivity of FeS, which
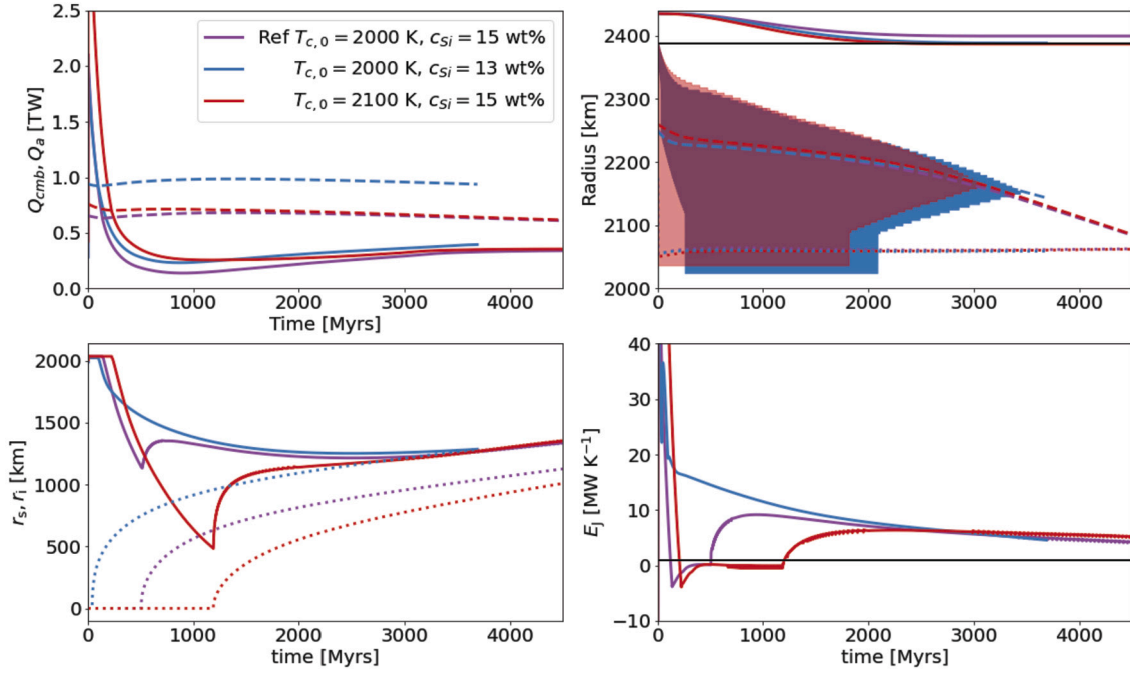
Fig. 4. Example core-mantle evolution for three models with $\eta_0 = 10^{21.5}$ Pa s and different core Si concentrations and initial core temperatures. Top left: Q_{cmb} (solid) and Q_a (dashed); top right: radius of base of the crust (solid), base of the upper thermal boundary layer (dashed), top of the lower thermal boundary layer (dotted), and partial melt region (filled colour) with a crustal thickness of 53 km indicated by the horizontal black line; bottom left: radius of the ICB (dotted) and base of the stable layer (solid); bottom right: entropy production (solid lines), with black horizontal line showing $E_J = 1$ MW K^{-1}. Default parameters in Table 1 are used.

is not accounted for when electrical conductivity is used with the Wiedemann-Franz law, is likely important. In this study, we ran simulations with $k_{FeS} = 5, 15, 20, 25$ W m^{-1} K^{-1} (Table 1), which is in general agreement with laboratory studies. The first value corresponds to the FeS-convecting regime, while the last three correspond to the FeS-conducting regime.

4. Results

4.1. No FeS layer

Fig. 4 shows three solutions that differ in the value of c_{Si} and $T_{c,0}$. The reference solution (purple line) matches the 4 constraints: it produces a present-day contraction of $\Delta r = 10$ km, $r_i = 1126$ km, $r_s = 1341$ km, a crustal thickness of 41 km, $T_c = 1987$, $T_m = 1927$ K and maintains a magnetic field for at least the last 3.8 Gyrs. In all cases, the CMB heat flow rapidly falls below Q_a and a thermally stratified layer begins to develop below the CMB in the first few hundred Myrs of the run (top left). Because $T_{c,0}$ is not far above the core liquidus, an inner core nucleates shortly after the onset of stratification (bottom left), which halts the growth of the stable layer due to the additional buoyancy at depth and provides latent heat that supplies crucial power to the dynamo. All cases produce a relatively thin crust and pervasive melting of the lower mantle until ~2 Ga. Crustal growth is fastest for the case with the hottest initial core temperature (red lines), which therefore produces the largest melt zone. Lowering c_{Si} from the reference value increases $T_{c,l}$ and so the inner core forms earlier. In Fig. 4, this result causes the entire core convection zone to disappear by 1 Ga and hence the model fails to maintain a magnetic field to the present day. Increasing $T_{c,0}$ from the reference value delays inner core formation such that there is insufficient entropy for dynamo action at 3.8 Ga. Clearly, decreasing $T_{c,0}$ would lead to an earlier inner core formation and failure of the model. The general time evolution of the solutions in Fig. 4 is consistent with that obtained by Knibbe and van Westrenen (2018, see their Figure 3).

Fig. 5 summarises the model behaviour as a function of the reference viscosity η_0, core Si concentration c_{Si}, and initial CMB temperature $T_{c,0}$

using the default parameters in Table 1. In this figure, all models that did not reach the present day have been excluded. These models are characterised essentially by a core silicon content $c_{Si} \leq 11$ wt%. In all models with $\eta_0 \leq 10^{21.5}$ Pa s, the time $t_{m,e}$ when melting ends is within the first 2-3 billion years, while no model predicts that new crust is currently being produced. $t_{m,e}$ is approximately independent of c_{Si} and $T_{c,0}$ and generally increases with η_0 because a more viscous mantle cools slower. Crustal thickness D_{cr} is determined by a competition between the melt volume, which increases with η_0, and the convective velocity, which decreases with η_0. At high η_0, the latter effect tends to dominate. The depth of the bulk convecting mantle $d - (\delta_u + \delta_l)$ decreases with increasing η_0 because of the thicker thermal boundary layers. The convection zone thickness also decreases with increasing Si concentration c_{Si} for two reasons. First, increasing c_{Si} increases the CMB radius, which decreases the mantle thickness. Second, adding light elements depresses the core melting point, which for fixed initial core temperature leads to later inner core formation, a thicker stable layer, and hence a reduced CMB heat flow (Fig. 4). The existence of a dynamo at 3.8 Ga is essentially determined by whether the inner core has formed, and this can be achieved with a range of combinations of $T_{c,0}$, c_{Si} and η_0. Maintaining dynamo action to the present day requires Si concentrations > 13 wt.% at low η_0 (< 10^{21} Pa s) to prevent the core from completely freezing, while at high η_0 a wider range of Si concentrations are viable. Contraction decreases significantly as η_0 increases because it depends strongly on the total amount of cooling (Grott et al., 2011; Tosi et al., 2013). For example, increasing the reference viscosity from 10^{20} to 10^{21} Pa s decreases contraction by a factor of about 2 (from about 30 to 15 km).

Fig. 6 shows some predictions from the models in Fig. 5. The present CMB temperature $T_c(r_c)$ increases with increasing η_0 due to reduced core cooling, and increases with decreasing c_{Si} due to earlier inner core growth and greater latent heat release that slows cooling. The present ICB radius decreases with increasing η_0, which decreases core cooling. For instance, for a core with 13 wt.% Si, increasing η_0 from 10^{20} to 10^{21} Pa s decreases the ICB radius by about 14%. The present ICB radius also decreases with increasing c_{Si}, because adding Si to the core increases the melting point depression, delaying inner core nucleation.
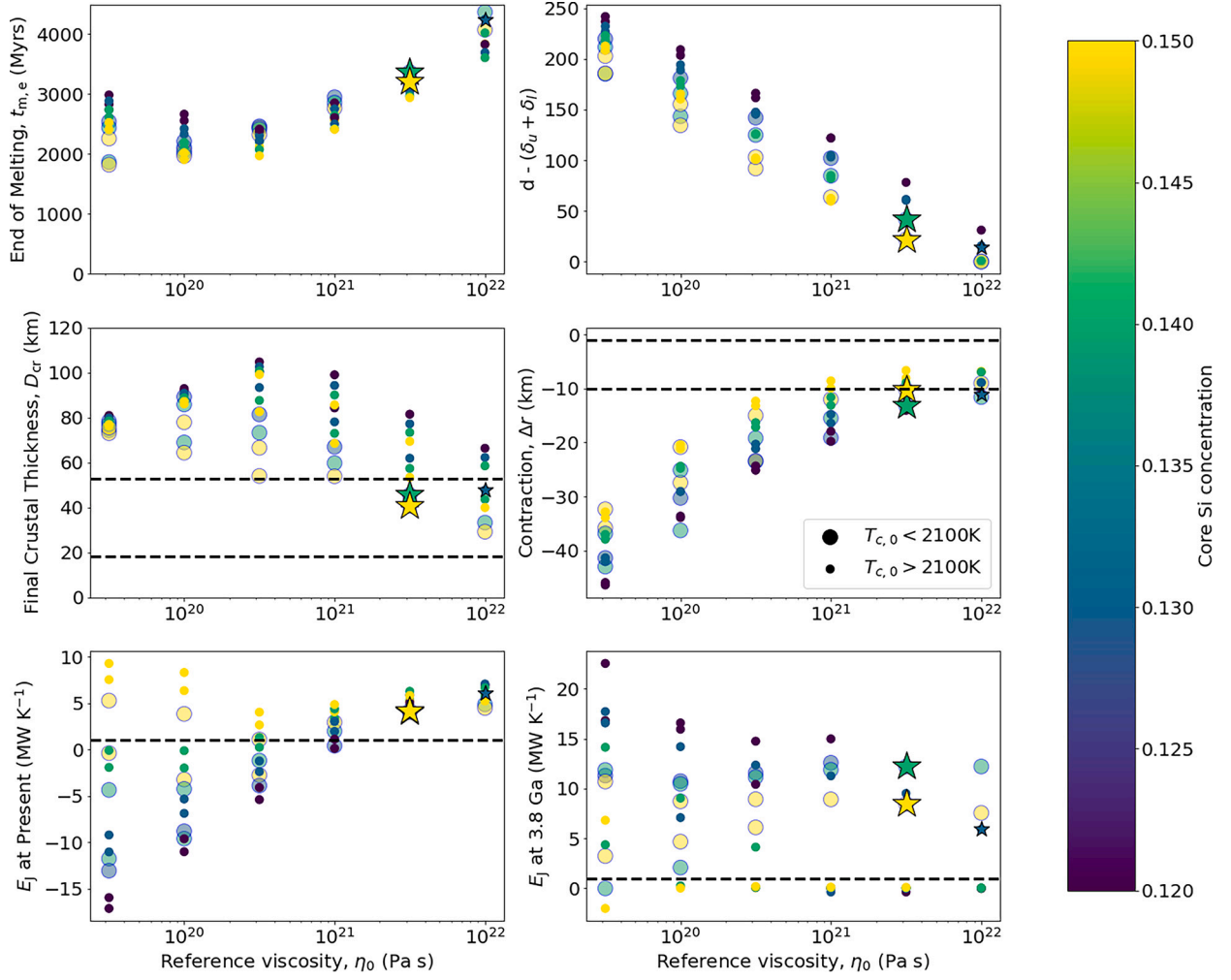
Fig. 5. Time when the mantle melt region closes, $t_{m,e}$ (top left), the difference between the thickness of the convective mantle and the sum of the boundary layer thicknesses, $d - (\delta_u + \delta_l)$ (top right), the final crustal thickness D_{cr} (middle left), the total radial contraction Δr (middle right) and E_J at the present day (bottom left) and at 3.8 Ga (bottom right), all as a function of the reference viscosity η_0, core Si concentration (colourbar), and initial CMB temperature (symbol size). Other parameters in Table 1 take their default values. Dashed lines on the plots of D_{cr} and Δr identify observationally-constrained ranges, while dashed lines on the E_J plots signify lower bounds for maintaining dynamo action. Stars denote models that simultaneously fulfil $\Delta r < 15$ km, a crustal thickness of $18 - 53$ km and $E_J > 1$ MW K^{-1} at present and 3.8 Ga, i.e. these models are close to satisfying the 4 criteria for successful models.

For a reference mantle viscosity value of 10^{20} Pa s, increasing the Si content from 13 to 15 wt.% decreases the ICB radius by about 10%. The stable layer thickness behaves in the opposite sense to the inner core radius because basal buoyancy from inner core growth erodes the stable layer (Fig. 4). These trends are consistent with those obtained in Knibbe and van Westrenen (2018). The predicted CMB dipole field strength is obtained by dividing the root mean square (RMS) field predicted by the scaling law by a factor of 15, which is consistent with outputs from geodynamo simulations (Davies et al., 2022). Modelled field strengths are higher than observed, consistent with findings from previous studies (Christensen, 2010; Davidson, 2013).

Starred symbols in Figs. 5 and 6 denote models that simultaneously fulfil $\Delta r < 15$ km (slightly broader than the observationally-derived bounds), a crustal thickness of $18 - 53$ km, and $E_J > 1$ MW K^{-1} at 3.8 Ga and the present day. We refer to these models as "marginally successful". Very few models match the observational constraints with the default parameters in Table 1, and those that do have a high mantle reference viscosity and core Si concentration. No marginally successful models are obtained with $k_m > 3$ W m^{-1} K^{-1}, though some are close. Large η_0 is required to match D_{cr} and Δr in our models; with $\eta_0 < 10^{21}$ Pa s, the mantle cools too quickly, producing a crust that is too thick and too much global contraction. Models that approximately

satisfy the contraction and crustal thickness constraints generally also satisfy the dynamo constraints and their E_J is a few times the minimum bound of 1 MW K^{-1}. In this suite of runs using the default parameters in Table 1 there is only one model (shown in Fig. 4) that matches the 4 constraints on global contraction, crustal thickness, and long-lived (early and present-day) dynamo generation.

Other factors such as regolith thickness D_{reg}, present-day ratio of mantle over crustal heat-producing elements (HPEs) f_{HPE}, and initial mantle temperature $T_{m,0}$ influence the global contraction and crustal thickness (e.g., Grott et al., 2011; Tosi et al., 2013). We therefore conducted another suite of runs focused on a high mantle reference viscosity η_0 ($10^{21}, 10^{21.5}, 10^{22}$ Pa s) and core Si concentration (11, 13, 15 wt%) since these are the conditions that best match the constraints (Fig. 5). We considered $D_{reg} = 1, 3, 5$ km, $f_{HPE} = 0.1, 0.33, 0.9$, $T_{m,0} = 1700, 1800, 1900$ K, and set the initial core temperature as increments of $dT = 100, 200, 300, 400$ K above $T_{m,0}$. Fig. 7 shows the final crustal thickness and contraction for this suite of runs, because these are the most stringent constraints (Fig. 5). Runs with $f_{HPE} = 0.9$ are not shown as they generally produce a crustal thickness that is too large (> 100 km) compared to present-day estimates (50 ± 12 km or less; e.g., Beuthe et al., 2020). Decreasing f_{HPE} compared to the default value of 0.33 decreases the crustal thickness by lowering the mantle temperature,
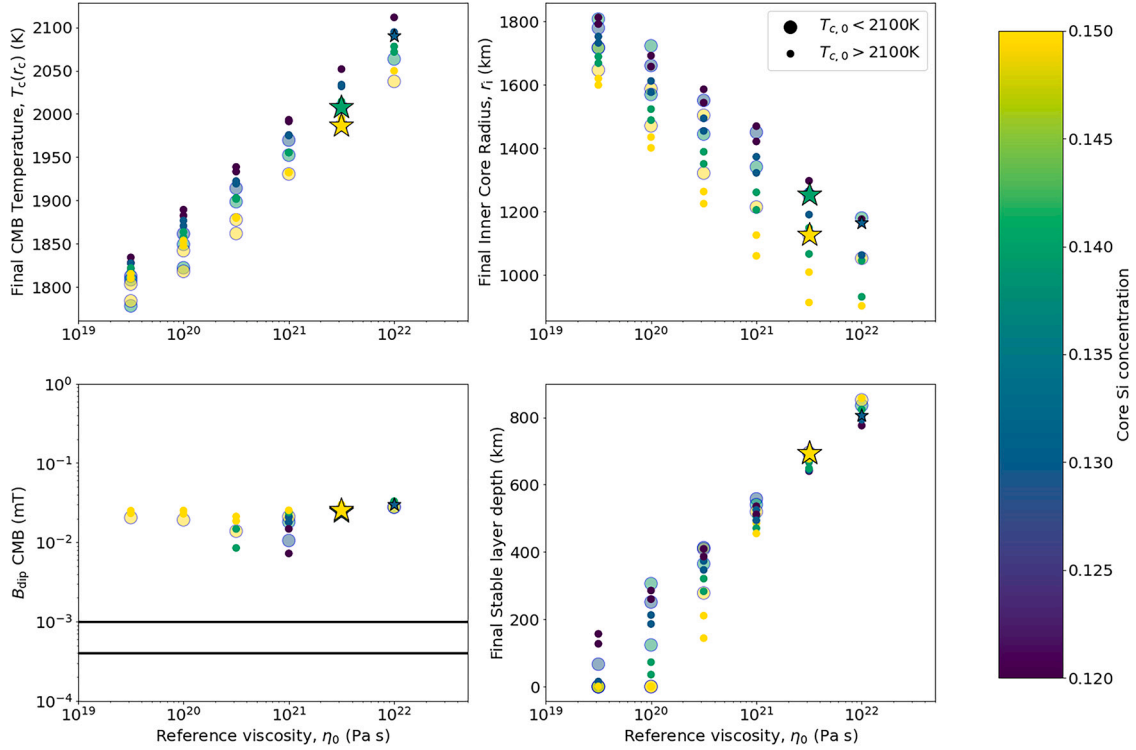
Fig. 6. Final CMB temperature (top left), final ICB radius (top right), present dipole field strength at the CMB B_{dip} (bottom left), and final depth of the stable layer (bottom right) all as a function of the reference viscosity η_0, core Si concentration (colourbar), and initial CMB temperature (symbol size and opacity). Other parameters in Table 1 take their default values. Solid lines on the plot of B_{dip} identify the observationally-constrained ranges, obtained using an axial dipole coefficient $g_1^0 = 200$ nT (Wardinski et al., 2019) and downward continuing to the top of the convecting core to obtain $B_{dip}^{obs} = g_1^0 (r_p/r_s)^3 \approx 4 - 10 \times 10^{-4}$ mT. Stars denote models that simultaneously fulfil $\Delta r < 15$ km, a crustal thickness of $18 - 53$ km and $E_J > 1$ MW K^{-1} at present and 3.8 Ga.
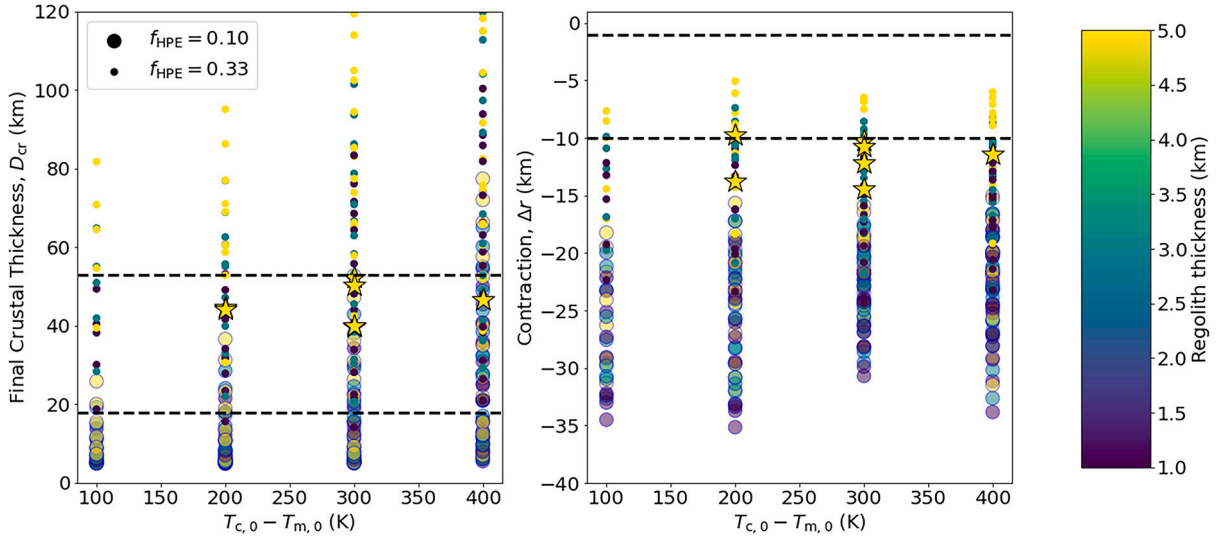

Fig. 7. Final crustal thickness D_{cr} (left) and the total radial contraction Δr (right) as a function of the initial core superheating, regolith thickness (colourbar), and ratio of mantle of crustal HPE element concentrations f_{HPE} (symbol size and opacity). Dashed lines identify observationally-constrained ranges. Stars denote models that simultaneously fulfil $\Delta r < 15$ km, a crustal thickness of $18 - 53$ km and $E_J > 1$ MW K^{-1}, i.e. these models are marginally successful. Marginally successful models have $T_{m,0} = 1700 - 1800$ K, $k_c(r_c) = 20 - 33$ W m^{-1} K^{-1}, present $r_i = 1115 - 1225$ km and present $r_s = 1215 - 1540$ km. Other parameters in Table 1 take their default values.

but also increases contraction due to increased cooling (Grott et al., 2011). A thinner regolith increases cooling, which decreases crustal production and increases contraction (Fig. 7). We conclude that, in our model, high values of the reference mantle viscosity, core Si concentration, regolith thickness, initial CMB temperature, volume fraction of extractable crustal components, and volume change on melting are required to match the chosen constraints.

4.2. Convecting FeS layer

Fig. 8 compares the reference solution in Fig. 4 to three runs with a convecting FeS layer of varying thickness (5, 50, 100 km). The heat flow time series shows that, aside from a brief early phase around 700 Ma, the FeS layer is superadiabatic at the CMB, consistent with the modelling assumptions. With our chosen parameterisation of $k(P, T, c)$, a
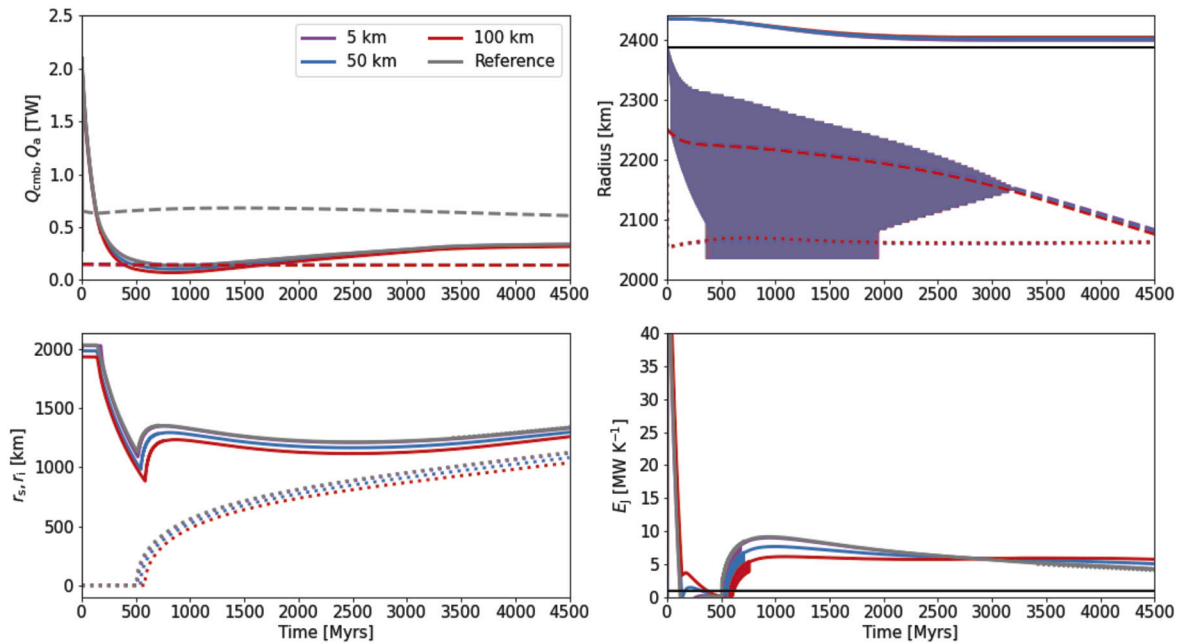
Fig. 8. Core-mantle evolution with a convecting FeS layer. All models share the parameters used for the reference case in Fig. 4, which is reproduced as a grey line in these plots. The three remaining models include an FeS layer of 5, 50, and 100 km thickness (equating to 0.49, 2.42 and 4.82 wt.% S in the core, respectively) with a thermal conductivity $k_{FeS} = 5$ W m^{-1} K^{-1} and density $\rho_{FeS} = 4800$ kg m^{-3}. Panels are the same as those in Fig. 4.

value of $k_{FeS} \leq 5$ W m^{-1} K^{-1} is required to produce an FeS layer that is approximately unstable to convection for all time. Thin FeS layers experience greater initial cooling than thicker layers because the layer cooling rate is $\propto V_{FeS}^{-3}$ (see equation (8)), which acts to reduce the CMB temperature and thus, Q_{cmb}. Lower CMB heat flow stifles subsequent cooling of the FeS layer to the extent that thinner layers cause a delay in the onset of thermal stratification compared to thicker layers. The time of inner core formation changes because the lower FeS layer density reduces the central pressure and hence the melting point; this effect is greater for thicker FeS layers. These effects combined mean that E_J is reduced in the period following inner core nucleation for runs with the thickest FeS layers because these cases have the thinnest convecting region. However, the combined effects of the FeS layer produce only modest changes to inner core nucleation and dynamo power that are confined to early times; the long-term evolution of cases with different FeS layer thickness becomes practically indistinguishable.

4.3. Conducting FeS layer

Fig. 9 compares the reference solution in Fig. 4 to three runs with a conducting FeS layer of varying thermal conductivity ($k_{FeS} = 15, 20, 25$ W m^{-1} K^{-1}) and a thickness of 100 km. Thinner layers have a smaller effect on the time evolution of the solution, i.e., the behaviour may be considered an extreme case designed to highlight the potential role of the FeS layer. All solutions are subadiabatic at the CMB after the initial period of rapid cooling, which is consistent with the modelling assumptions. Decreasing k_{FeS} slows core cooling, which marginally delays the onset of stable layer and inner core formation by < 50 Myrs. The dynamo entropy is also marginally reduced with increasing k_{FeS}, but by such a small amount that the effect would be imperceptible in observations. Therefore, like the convecting FeS case, the long-term evolution of the core-mantle system is almost indistinguishable between cases with and without a conducting FeS layer.

5. Discussion and conclusions

We have compared large suites of coupled core-mantle thermal-magnetic evolution models with and without a liquid FeS layer to observations of Mercury's magnetic field evolution, crustal thickness and

total radial contraction. Of the few models that successfully satisfy these constraints, all have reference mantle viscosities $\eta_0 > 10^{21}$ Pa s, with values of bulk mantle viscosity in the range $5 \times 10^{19} - 3 \times 10^{21}$ Pa s and a lower mantle viscosity in the range $2 \times 10^{19} - 7 \times 10^{19}$ Pa s. The high viscosity slows planetary cooling and therefore limits contraction and crustal thickness as found in previous studies (e.g., Tosi et al., 2013). The inner core forms early in history in all our successful model runs, which is required by the high melting point of the Fe-Si alloy and is crucial for maintaining a long-lived dynamo through the latent heat of crystallisation. The addition of an FeS layer has a negligible effect on the inner core formation time (< 50 Myrs) and the long-term thermal and magnetic evolution of the core.

Our successful solutions maintain convection in both mantle and core until the present day. The persistence of mantle convection is known to be sensitive to the thermal evolution and model parameters (Hauck et al., 2004; Grott et al., 2011). Our results are consistent with Michel et al. (2013), who found that convection can be persistent in a mantle as thin as 300 km.

The minimum global contraction Δr in our models is around 9 km, which matches the upper end of observationally-constrained values (Byrne et al., 2014) but never reaches the low values of $1 - 2$ km suggested by some studies (Watters, 2021). Our estimates rely on the density difference between solid and liquid iron $\rho_S - \rho_L$ and the volume change on melting $\delta V / V$. These quantities are poorly known and trade off such that (within the uncertainties) a lower $\rho_S - \rho_L$ can be compensated by a lower $\delta V / V$ to give essentially the same total contraction. However, with the values of $\delta V / V$ and $\rho_S - \rho_L$ we have selected, Δr is only marginally compatible with observations. Nevertheless, our results show that matching the observed Δr is possible without adding physical effects to the model such as water and radiogenic element loss from heat-piping (Peterson et al., 2021). Including these effects would bring our Δr closer to the mid-lower end of the observed range. We note that the time evolution of Δr in our successful models (see Supplementary Figure 4) suggests that significant contraction did not begin until ~ 3 Gyrs ago, which is somewhat later that inferences from recent tectonic studies (e.g., Giacomini et al., 2020).

We assumed a required crustal thickness range of $D_{cr} = 35 \pm 18$ km but also considered more conservative estimates. Our successful models
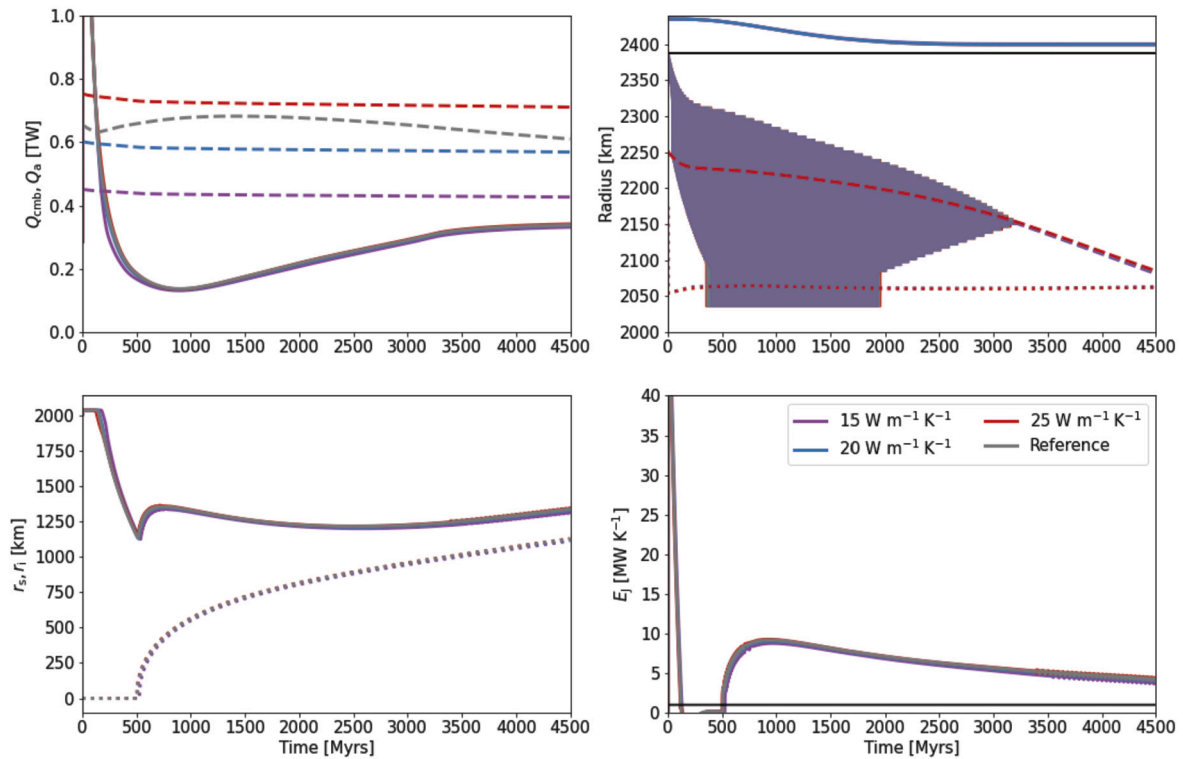
Fig. 9. Core-mantle evolution with a conducting FeS layer. All models share the parameters used for the reference case in Fig. 4, which is reproduced as a grey line in these plots. The three FeS models include an FeS layer of 100 km thickness (equating to 4.82 wt.% FeS) with a thermal conductivity $k_{FeS} = 15, 20$ and 25 W m^{-1} K^{-1}. Panels are the same as those in Fig. 4.

yield a minimum present-day $D_{cr} \sim 40$ km, which is in good agreement with the range provided by Beuthe et al. (2020) but is slightly above the more restrictive bounds of Padovan et al. (2015) and Sori (2018). Models with $D_{cr} < 40$ km are associated with more rapid cooling and produce a total radial contraction that is much larger than the observationally-inferred values.

In addition to Si, small amounts of C might be present in the core (e.g., Tao and Fei, 2021). The presence of graphite at the surface suggests that the planet might be carbon saturated (Vander Kaaden et al., 2020; Lark et al., 2022). Light elements in general are expected to lower the melting temperature of the metallic core, though this effect might be negligible if they are present in small amount. Any decrease to the liquidus temperature will delay onset of inner core crystallisation, but if the effect is large enough to shift inner core formation to earlier than 3.8 Ga our model would predict insufficient power available to the early dynamo. At present the liquidus depression caused by multiple light elements is not well constrained, requiring further experimental data.

Future modelling work is needed to explore scenarios that consider a significant size reduction of Mercury following rapid collisional stripping of the silicate portion of the planet by giant impacts (Benz et al., 1988). This hypothesis has been proposed to explain the large core/mantle ratio, but has not been tested in thermal history models. The shape of the core melting gradient will change in a large proto-Mercury, spanning different *PT* ranges than in our models. As a result, the intersection of the adiabat and the melting curve might occur at a different depth in the core, potentially leading to other crystallisation regimes, such as a snowing core (Dumberry and Rivoldini, 2015; Davies and Pommier, 2018).

Our successful solutions make predictions about the present-day size of Mercury's inner core and thermally stable layer. Clearly, uncertainties on some key input parameters and model parameterisations (see discussions in Grott et al., 2011; Peterson et al., 2021) mean that only loose bounds can be obtained. Care is also needed because of the small number of successful models. Of the thousands of runs, only four

successful models were obtained, which yielded $1110 < r_i < 1160$ km and $1220 < r_s < 1340$ km. Allowing a larger crustal thickness D_{cr} of 62 km (the maximum value suggested by Beuthe et al., 2020) yields six successful runs with $1090 < r_i < 1160$ and $1220 < r_s < 1355$ km, a marginal difference. Retaining this larger D_{cr} and omitting the constraint on the ancient dynamo while still requiring $\Delta r \leq 10$ km and $E_J > 1$ MW K^{-1} at present yields ten successful runs with $990 < r_i < 1160$ km and $1220 < r_s < 1360$ km, similar to the range obtained in Fig. 6 for the "marginally successful" models. Overall the model results are consistent with a present ICB radius of ~1000-1200 km and present stable layer thickness of ~500-700 km with preferred values towards the centre of these ranges. The inferred present ICB is towards the upper end of predictions from recent interior structure models (e.g., Genova et al., 2019; Steinbrügge et al., 2021).

A thermally stable layer below the CMB forms early in all of our successful models, similar to Knibbe and van Westrenen (2018). Layer growth is initially rapid and subsequently stifled by growth of the inner core. Nevertheless, this behaviour inevitably leads to a stable layer of $500 - 700$ km at the present-day. This thick layer keeps the CMB warm, with a present temperature of ~1900 K in our models, which is nevertheless below the mantle solidus and consistent with the absence of present-day volcanism. Combining the constraints on r_i and r_s, our results suggest that the present-day dynamo is generated in a thin shell of $100 - 500$ km underlying a thick thermally stable layer and surrounding the inner core. These predictions can be tested by future modelling efforts, new experimental data, and observations by BepiColombo.

CRediT authorship contribution statement

Christopher J. Davies: Writing – review & editing, Writing – original draft, Supervision, Software, Resources, Methodology, Investigation, Funding acquisition, Formal analysis, Conceptualization. **Anne Pommier:** Writing – review & editing, Investigation, Funding acquisition, Formal analysis, Data curation, Conceptualization. **Sam Green-**

wood: Validation, Software, Methodology, Investigation. **Alfred Wilson:** Writing – review & editing, Software, Methodology, Investigation, Formal analysis.

Appendix A. Mantle melting

The parameterisation of mantle melting is identical to that used in Knibbe and van Westrenen (2018) and is reproduced here for convenience. The crustal growth rate is given by

$$\frac{dD_{cr}}{dt} = u m_a \frac{V_a}{4\pi r_p^2}, \qquad (16)$$

where D_{cr} is the crustal thickness, $r_p = 2440$ km is the planetary radius, and the convective velocity $u = u_0(Ra/Ra_c)^{2/3}$ with $Ra_c = 450$ the critical value of the Rayleigh number Ra. The volume V_a is defined as the region where the mantle temperature exceeds the solidus temperature $T_{m,s}$, and m_a is the average melt fraction in V_a.

V_a and m_a depend on the mantle solidus and liquidus. The mantle solidus is given by

$$T_{m,s} = T_{m,s,0} + \frac{D_{cr}}{D_{ref}} \Delta T_{m,s}, \qquad (17)$$

where

$$T_{m,s,0} = 1421 + 177P - 12.2P^2 \qquad (18)$$

(Namur et al., 2016), $\Delta T_{m,s} = 150$ K is the solidus difference between the initial mantle composition and that depleted in crustal material, and

$$D_{ref} = \frac{0.2}{3} \frac{r_p^3 - r_c^3}{r_p^2}. \qquad (19)$$

The definition of D_{ref} reflects the assumption that $T_{m,s}$ stops increasing when around 20% mantle volume of crustal material is formed (Morschhauser et al., 2011).

The mantle liquidus is given by

$$T_{m,l} = 2036 + 57.46P - 3.487P^2 + 0.0769P^3 \qquad (20)$$

(Morschhauser et al., 2011).

The mean melt fraction in the melt volume V_a is given by

$$m_a = \frac{1}{V_a} \int \frac{T(r) - T_{m,s}(r)}{T_{m,l}(r) - T_{m,s}(r)} dV \qquad (21)$$

Appendix B. Mantle radiogenic heat production

Radiogenic heating is produced by the decay of potassium, uranium, and thorium. The heating rates H_m^i (W/kg) of ^{40}K, ^{235}U, ^{238}U, and ^{232}Th at 4.3 Ga are respectively 10^{-11}, 7×10^{-12}, 3.5×10^{-12}, and 2×10^{-12} (see Padovan et al., 2015, figure 3). Padovan et al. (2015) use mass balance to estimate maximum mantle abundances c_m of 265 ppm ^{40}K, 69 ppb ^{232}Th, and 20 ppb U, while the surface concentrations c_{cr} are taken from Peplowski et al. (2011, 2012) and are 1288 ppm ^{40}K, 155 ppb ^{232}Th, and 90 ppb U respectively. The heating rates in the crust at the surface are $H_{cr}^i = H_m^i c_{cr}^i / c_m^i$ for each isotope i. Note that the values in Knibbe and van Westrenen (2018) below their equation B.3 refer to the bulk mantle and not the crust.

The total radiogenic heat production in the mantle and crust as a function of time t is

$$Q_{r,tot}(t) = Q_{r,c}(t) + Q_{r,m}(t) = \sum_i V_{cr}(t)\rho_{cr} H_{cr}^i(t) + V_{ml}(t)\rho_m H_{ml}^i(t) \qquad (22)$$

$$= \sum_i V_{cr}(t)\rho_{cr} H_{cr}^i(t) + V_{ml}(t)\rho_m f_{HPE} H_{cr}^i(t), \qquad (23)$$

where $f_{HPE} = H_{ml}/H_{cr}$ is ratio of mantle to crustal abundances of heat-producing elements (HPEs), $V_{cr}(t) = 4\pi(r_p^3 - r_{cr}^3)/3$ is the crustal volume, $V_m = 4\pi(r_1^3 - r_c^3)/3$ is the bulk mantle volume, $V_1 = 4\pi(r_{cr}^3 - r_1^3)/3$ is the lithosphere volume, and $V_{ml} = V_m + V_1$. The heating rate in the crust for each isotope i evolves in time according to

$$H_{cr}^i(t) = H_{cr}^i(t = 4.3\text{Ga}) \exp\left(\frac{\ln(2)(4.3\text{Ga} - t)}{t_{1/2}^i}\right) \qquad (24)$$

where the $t_{1/2}^i$ are the isotopic half lives. The heating rate of the mantle can be found using the total heat produced, the crustal heating rate, and the mass of the mantle (excluding the lithosphere):

$$H_{ml}^i(t) = \frac{Q_{r,tot}(t) - V_{cr}(t)\rho_{cr} H_{cr}^i(t)}{V_m(t)\rho_m}. \qquad (25)$$

In the main text $Q_{r,m}(t)$ is denoted by Q_r for convenience.

Appendix C. Supplementary material

Supplementary material related to this article can be found online at https://doi.org/10.1016/j.epsl.2024.118812.

References

Anderson, B.J., Johnson, C.L., Korth, H., Purucker, M.E., Winslow, R.M., Slavin, J.A., Solomon, S.C., McNutt Jr., R.L., Raines, J.M., Zurbuchen, T.H., 2011. The global magnetic field of Mercury from MESSENGER orbital observations. Science 333 (6051), 1859–1862.

Benz, W., Slattery, W.L., Cameron, A., 1988. Collisional stripping of Mercury's mantle. Icarus 74, 516–528.

Bertone, Stefano, Mazarico, Erwan, Barker, M.K., Goossens, Sander, Sabaka, T.J., Neumann, G.A., Smith, David E., 2021. Deriving Mercury geodetic parameters with altimetric crossovers from the Mercury Laser Altimeter (MLA). J. Geophys. Res., Planets 126 (4), e2020JE006683.

Beuthe, M., Charlier, B., Namur, O., Rivoldini, A., Van Hoolst, T., 2020. Mercury's crustal thickness correlates with lateral variations in mantle melt production. Geophys. Res. Lett. 47, e2020GL087261.

Boujibar, A., Andrault, D., Bouhifd, M.A., Bolfan-Casanova, N., Devidal, J.L., Trcera, N., 2014. Metal–silicate partitioning of sulphur, new experimental and thermodynamic constraints on planetary accretion. Earth Planet. Sci. Lett. 391, 42–54.

Boujibar, A., Habermann, M., Righter, K., Ross, D.K., Pando, K., Righter, M., Chidester, B.A., Danielson, L.R., 2019. U, Th, and K partitioning between metal, silicate, and sulfide and implications for Mercury's structure, volatile content, and radioactive heat production. Am. Mineral. 104, 1221–1237.

Boukaré, C.-E., Parman, S.W., Parmentier, E.M., Anzures, B.A., 2019. Production and preservation of sulfide layering in Mercury's mantle. J. Geophys. Res., Planets 124, 3354–3372.

Byrne, P.K., Klimczak, C., Celâl Şengör, A., Solomon, S.C., Watters, T.R., Hauck II, S.A., 2014. Mercury's global contraction much greater than earlier estimates. Nat. Geosci. 7, 301–307.

Byrne, P.K., Ostrach, L.R., Fassett, C.I., Chapman, C.R., Denevi, B.W., Evans, A.J., Klimczak, C., Banks, M.E., Head, J.W., Solomon, S.C., 2016. Widespread effusive volcanism on Mercury likely ended by about 3.5 Ga. Geophys. Res. Lett. 43, 7408–7416.

Cartier, C., Namur, O., Nittler, L., Weider, S., Crapster-Pregont, E., Vorburger, A., Frank, E., Charlier, B., 2020. No FeS layer in Mercury? Evidence from Ti/Al measured by MESSENGER. Earth Planet. Sci. Lett. 534, 116108.

Chabot, N.L., Wollack, E.A., Klima, R.L., Minitti, M.E., 2014. Experimental constraints on Mercury's core composition. Earth Planet. Sci. Lett. 390, 199–208.

Christensen, U., 2010. Dynamo scaling laws and applications to the planets. Space Sci. Rev. 152, 565–590.

Christensen, U.R., 2006. A deep dynamo generating Mercury's magnetic field. Nature 444, 1056–1058. https://doi.org/10.1038/nature05342.

Davidson, P., 2013. Scaling laws for planetary dynamos. Geophys. J. Int. 195, 67–74.

Davies, C.J., Pommier, A., 2018. Iron snow in the Martian core? Earth Planet. Sci. Lett. 481, 189–200. https://doi.org/10.1016/j.epsl.2017.10.026.

Davies, C.J., Bono, R.K., Meduri, D.G., Aubert, J., Greenwood, S., Biggin, A.J., 2022. Dynamo constraints on the long-term evolution of Earth's magnetic field strength. Geophys. J. Int. 228, 316–336.

De Koker, N., Steinle-Neumann, G., Vlček, V., 2012. Electrical resistivity and thermal conductivity of liquid Fe alloys at high P and T, and heat flux in Earth's core. Proc. Natl. Acad. Sci. USA 109, 4070–4073. https://doi.org/10.1073/pnas.1111841109.

Dobrosavljevic, V.V., Zhang, D., Sturhahn, W., Zhao, J., Toellner, T.S., Chariton, S., Prakapenka, V.B., Pardo, O.S., Jackson, J.M., 2022. Melting and phase relations of Fe-Ni-Si determined by a multi-technique approach. Earth Planet. Sci. Lett. 584, 117358.

Dumberry, M., Rivoldini, A., 2015. Mercury's inner core size and core-crystallization regime. Icarus 248, 254–268. https://doi.org/10.1016/j.icarus.2014.10.038.

Fassett, C.I., 2016. Analysis of impact crater populations and the geochronology of planetary surfaces in the inner solar system. J. Geophys. Res., Planets 121, 1900–1926.

Fischer, R.A., Campbell, A.J., Reaman, D.M., Miller, N.A., Heinz, D.L., Dera, P., Prakapenka, V.B., 2013. Phase relations in the Fe–FeSi system at high pressures and temperatures. Earth Planet. Sci. Lett. 373, 54–64.

Freitas, D., Monteux, J., Andrault, D., Manthilake, G., Mathieu, A., Schiavi, F., Cluzel, N., 2021. Thermal conductivities of solid and molten silicates: implications for dynamos in Mercury-like proto-planets. Phys. Earth Planet. Inter. 312, 106655.

Genova, A., Goossens, S., Mazarico, E., Lemoine, F.G., Neumann, G.A., Kuang, W., Sabaka, T.J., Hauck, S.A., Smith, D.E., Solomon, S.C., et al., 2019. Geodetic evidence that Mercury has a solid inner core. Geophys. Res. Lett. 46, 3625–3633.

Giacomini, L., Massironi, M., Galluzzi, V., Ferrari, S., Palumbo, P., 2020. Dating long thrust systems on Mercury: new clues on the thermal evolution of the planet. Geosci. Front. 11, 855–870.

Goossens, S., Renaud, J.P., Henning, W.G., Mazarico, E., Bertone, S., Genova, A., 2022. Evaluation of recent measurements of Mercury's moments of inertia and tides using a comprehensive Markov Chain Monte Carlo method. Planet. Sci. J. 3, 37.

Greenwood, S., Davies, C.J., Mound, J.E., 2021a. On the evolution of thermally stratified layers at the top of Earth's core. Phys. Earth Planet. Inter. 318, 106763.

Greenwood, S., Davies, C.J., Pommier, A., 2021b. Influence of thermal stratification on the structure and evolution of the Martian core. Geophys. Res. Lett. 48, e2021GL095198.

Grott, M., Breuer, D., Laneuville, M., 2011. Thermo-chemical evolution and global contraction of Mercury. Earth Planet. Sci. Lett. 307, 135–146.

Gubbins, D., 1975. Can the Earth's magnetic field be sustained by core oscillations? Geophys. Res. Lett. 2, 409–412.

Hauck II, S.A., Dombard, A.J., Phillips, R.J., Solomon, S.C., 2004. Internal and tectonic evolution of Mercury. Earth Planet. Sci. Lett. 222, 713–728.

Hauck, S.A., Margot, J.L., Solomon, S.C., Phillips, R.J., Johnson, C.L., Lemoine, F.G., Mazarico, E., McCoy, T.J., Padovan, S., Peale, S.J., et al., 2013. The curious case of Mercury's internal structure. J. Geophys. Res., Planets 118, 1204–1220.

Hofmeister, A.M., Whittington, A.G., Pertermann, M., 2009. Transport properties of high albite crystals, near-endmember feldspar and pyroxene glasses, and their melts to high temperature. Contrib. Mineral. Petrol. 158, 381–400.

Hsieh, W.P., Goncharov, A.F., Labrosse, S., Holtgrewe, N., Lobanov, S.S., Chuvashova, I., Deschamps, F., Lin, J.F., 2020. Low thermal conductivity of iron-silicon alloys at Earth's core conditions with implications for the geodynamo. Nat. Commun. 11, 3332.

Hsieh, W.P., Deschamps, F., Tsao, Y.C., Yoshino, T., Lin, J.F., 2024. A thermally conductive martian core and implications for its dynamo cessation. Sci. Adv. 10, eadk1087.

Johnson, C.L., Phillips, R.J., Purucker, M.E., Anderson, B.J., Byrne, P.K., Denevi, B.W., Feinberg, J.M., Hauck, S.A., Head III, J.W., Korth, H., et al., 2015. Low-altitude magnetic field measurements by MESSENGER reveal Mercury's ancient crustal field. Science 348, 892–895.

Knibbe, J.S., Rivoldini, A., Luginbuhl, S., Namur, O., Charlier, B., Mezouar, M., Sifre, D., Berndt, J., Kono, Y., Neuville, D., et al., 2021. Mercury's interior structure constrained by density and P-wave velocity measurements of liquid Fe-Si-C alloys. J. Geophys. Res., Planets 126, e2020JE006651.

Knibbe, J.S., Van Hoolst, T., 2021. Modelling of thermal stratification at the top of a planetary core: application to the cores of Earth and Mercury and the thermal coupling with their mantles. Phys. Earth Planet. Inter. 321, 106804.

Knibbe, J.S., van Westrenen, W., 2018. The thermal evolution of Mercury's Fe–Si core. Earth Planet. Sci. Lett. 482, 147–159. https://doi.org/10.1016/j.epsl.2017.11.006.

Kuwayama, Y., Hirose, K., 2004. Phase relations in the system Fe-FeSi at 21 GPa. Am. Mineral. 89, 273–276.

Lark, L., Parman, S., Huber, C., Parmentier, E., Head III, J., 2022. Sulfides in Mercury's mantle: implications for Mercury's interior as interpreted from moment of inertia. Geophys. Res. Lett. 49, e2021GL096713.

Malavergne, V., Toplis, M.J., Berthet, S., Jones, J., 2010. Highly reducing conditions during core formation on Mercury: implications for internal structure and the origin of a magnetic field. Icarus 206, 199–209.

Manglik, A., Wicht, J., Christensen, U.R., 2010. A dynamo model with double diffusive convection for Mercury's core. Earth Planet. Sci. Lett. 289, 619–628. https://doi.org/10.1016/j.epsl.2009.12.007.

Manthilake, G., Chantel, J., Monteux, J., Andrault, D., Bouhifd, M.A., Bolfan Casanova, N., Boulard, E., Guignot, N., King, A., Itié, J.P., 2019. Thermal conductivity of FeS and its implications for Mercury's long-sustaining magnetic field. J. Geophys. Res., Planets 124, 2359–2368.

Margot, J.L., Peale, S., Jurgens, R., Slade, M., Holin, I., 2007. Large longitude libration of Mercury reveals a Molten core. Science 316, 710–714.

Margot, Jean-Luc, Peale, Stanton J., Solomon, Sean C., Hauck, Steven A., Ghigo, Frank D., Jurgens, Raymond F., Yseboodt, Marie, Giorgini, Jon D., Padovan, Sebastiano, Campbell, Donald B., 2012. Mercury's moment of inertia from spin and gravity data. J. Geophys. Res., Planets 117, E12.

Margot, J.L., Hauck, S.A., Mazarico, E., Padovan, S., Peale, S.J., 2018. Mercury's internal structure. In: Mercury. The View After MESSENGER, pp. 85–113.

McCubbin, F.M., Riner, M.A., Vander Kaaden, K.E., Burkemper, L.K., 2012. Is Mercury a volatile-rich planet? Geophys. Res. Lett. 39.

Michel, N.C., Hauck, S.A., Solomon, S.C., Phillips, R.J., Roberts, J.H., Zuber, M.T., 2013. Thermal evolution of Mercury as constrained by MESSENGER observations. J. Geophys. Res., Planets 118, 1033–1044.

Morard, G., Katsura, T., 2010. Pressure–temperature cartography of Fe–S–Si immiscible system. Geochim. Cosmochim. Acta 74, 3659–3667.

Morschhauser, A., Grott, M., Breuer, D., 2011. Crustal recycling, mantle dehydration, and the thermal evolution of Mars. Icarus 212, 541–558.

Namur, O., Charlier, B., Holtz, F., Cartier, C., McCammon, C., 2016. Sulfur solubility in reduced mafic silicate melts: implications for the speciation and distribution of sulfur on Mercury. Earth Planet. Sci. Lett. 448, 102–114.

Nimmo, F., 2015. Energetics of the core. In: Treatise on Geophysics, vol. 8, second edition, pp. 27–55.

Nishida, K., Ohtani, E., Urakawa, S., Suzuki, A., Sakamaki, T., Terasaki, H., Katayama, Y., 2011. Density measurement of liquid FeS at high pressures using synchrotron X-ray absorption. Am. Mineral. 96, 864–868.

Padovan, S., Wieczorek, M.A., Margot, J.L., Tosi, N., Solomon, S.C., 2015. Thickness of the crust of Mercury from geoid-to-topography ratios. Geophys. Res. Lett. 42, 1029–1038.

Peplowski, P.N., Evans, L.G., Hauck, S.A., McCoy, T.J., Boynton, W.V., Gillis-Davis, J.J., Ebel, D.S., Goldsten, J.O., Hamara, D.K., Lawrence, D.J., et al., 2011. Radioactive elements on Mercury's surface from MESSENGER: implications for the planet's formation and evolution. Science 333, 1850–1852.

Peplowski, P.N., Lawrence, D.J., Rhodes, E.A., Sprague, A.L., McCoy, T.J., Denevi, B.W., Evans, L.G., Head, J.W., Nittler, L.R., Solomon, S.C., et al., 2012. Variations in the abundances of potassium and thorium on the surface of Mercury: results from the MESSENGER gamma-ray spectrometer. J. Geophys. Res., Planets 117.

Peterson, G.A., Johnson, C.L., Jellinek, A.M., 2021. Thermal evolution of Mercury with a volcanic heat-pipe flux: reconciling early volcanism, tectonism, and magnetism. Sci. Adv. 7, eabh2482.

Pirotte, H., Cartier, C., Namur, O., Pommier, A., Zhang, Y., Berndt, J., Klemme, S., Charlier, B., 2023. Internal differentiation and volatile budget of Mercury inferred from the partitioning of heat-producing elements at highly reduced conditions. Icarus 405, 115699.

Pommier, A., Leinenweber, K., Tran, T., 2019. Mercury's thermal evolution controlled by an insulating liquid outermost core? Earth Planet. Sci. Lett. 517, 125–134.

Rivoldini, A., Van Hoolst, T., Verhoeven, O., 2009. The interior structure of Mercury and its core sulfur content. Icarus 201, 12–30.

Saxena, S., Pommier, A., Tauber, M., 2021. Iron sulfides and anomalous electrical resistivity in cratonic environments. J. Geophys. Res., Solid Earth 126, e2021JB022297.

Smith, D.E., Zuber, M.T., Phillips, R.J., Solomon, S.C., Hauck, S.A., Lemoine, F.G., Mazarico, E., Neumann, G.A., Peale, S.J., Margot, J.L., et al., 2012. Gravity field and internal structure of Mercury from MESSENGER. Science 336, 214–217.

Sori, M.M., 2018. A thin, dense crust for Mercury. Earth Planet. Sci. Lett. 489, 92–99.

Steinbrügge, G., Dumberry, M., Rivoldini, A., Schubert, G., Cao, H., Schroeder, D., Soderlund, K., 2021. Challenges on Mercury's interior structure posed by the new measurements of its obliquity and tides. Geophys. Res. Lett. 48, e2020GL089895.

Takahashi, F., Shimizu, H., Tsunakawa, H., 2019. Mercury's anomalous magnetic field caused by a symmetry-breaking self-regulating dynamo. Nat. Commun. 10, 208.

Tao, R., Fei, Y., 2021. High-pressure experimental constraints of partitioning behavior of Si and S at the Mercury's inner core boundary. Earth Planet. Sci. Lett. 562, 116849.

Tosi, N., Grott, M., Plesa, A.C., Breuer, D., 2013. Thermochemical evolution of Mercury's interior. J. Geophys. Res., Planets 118, 2474–2487.

Urakawa, S., Someya, K., Terasaki, H., Katsura, T., Yokoshi, S., Funakoshi, K.i., Utsumi, W., Katayama, Y., Sueda, Y.i., Irifune, T., 2004. Phase relationships and equations of state for FeS at high pressures and temperatures and implications for the internal structure of Mars. Phys. Earth Planet. Inter. 143, 469–479.

Vander Kaaden, K.E., McCubbin, F.M., Turner, A.A., Ross, D.K., 2020. Constraints on the abundances of carbon and silicon in Mercury's core from experiments in the Fe-Si-C system. J. Geophys. Res., Planets 125, e2019JE006239.

Wardinski, I., Langlais, B., Thébault, E., 2019. Correlated time-varying magnetic fields and the core size of Mercury. J. Geophys. Res., Planets 124, 2178–2197.

Watters, T.R., 2021. A case for limited global contraction of Mercury. Commun. Earth Environ. 2, 9.

Xu, R., Xiao, Z., Wang, Y., Cui, J., 2024. Less than one weight percent of graphite on the surface of Mercury. Nat. Astron., 1–10.

Xu, Y., Shankland, T.J., Linhardt, S., Rubie, D.C., Langenhorst, F., Klasinski, K., 2004. Thermal diffusivity and conductivity of olivine, wadsleyite and ringwoodite to 20 GPa and 1373 K. Phys. Earth Planet. Inter. 143, 321–336.

Zhang, Y., Yoshino, T., Yoneda, A., Osako, M., 2019. Effect of iron content on thermal conductivity of olivine with implications for cooling history of rocky planets. Earth Planet. Sci. Lett. 519, 109–119.

Zolotov, M.Y., Sprague, A.L., Hauck, S.A., Nittler, L.R., Solomon, S.C., Weider, S.Z., 2013. The redox state, FeO content, and origin of sulfur-rich magmas on Mercury. J. Geophys. Res., Planets 118, 138–146.